8 Collective Behaviour of Vertically Aligned Carbon Nanotubes: from a Single Tube towards Complex Networks

Siddhartha Pathak

Center for Integrated Nanotechnologies, Los Alamos National Laboratory, Los Alamos, NM 87545, USA

8.1. Definition

In this chapter we discuss the mechanical behaviour of vertically aligned carbon nanotubes (VACNTs) also known as carbon nanotube (CNT) arrays, bundles, brushes, foams, forests, mats, and turfs. VACNTs are complex, hierarchical structures of intertwined tubes arrayed in a nominally vertical alignment due to their perpendicular growth from a stiff substrate. They are a unique class of materials having many of the desirable thermal, electrical, and mechanical properties of individual carbon nanotubes, while exhibiting these properties through the collective interaction of thousands of tubes on a macroscopic scale.

8.2. Introduction

While individual CNTs have been announced as the strongest material known (Treacy et al. 1996) and have shown extremely high strength and Young's modulus in tensile tests on individual tubes (Treacy et al. 1996, Min-Feng et al. 2000), VACNTs are more likely to find use in applications requiring large compliance and deformability (Cao et al. 2005, Gogotsi 2006). Examples of these include microelectromechanical systems (MEMS) and impact mitigation/energy absorption, where they are promising candidates for their multifunctional nature, wide ranging thermal stability, well-defined large surface area, and relative ease of manufacture (Cao et al. 2005). A proper understanding of the collective mechanical behaviour of these structures, especially instabilities leading to buckling and inhomogeneity's which weaken mechanical performance, is thus of great importance for their design and success in these and other future applications.

VACNTs are distinct from other CNT structures (Salvetat et al. 2006) in that the tubes that make up the material grow perpendicularly to the support substrate, making them *nominally* vertically aligned. An important characteristic all VACNTs share is that the tubes themselves are long enough to become intertwined with each other during the growth process, leading to a highly complex and hierarchical

microstructure with distinct organizational details at different magnification levels. This is in contrast to arrays of vertically aligned CNTs that are short and/or sparse enough that each CNT stands alone (Waters et al. 2004, Waters et al. 2005). Figure 8.1 show the complex hierarchical nature of the VACNT microstructure with their
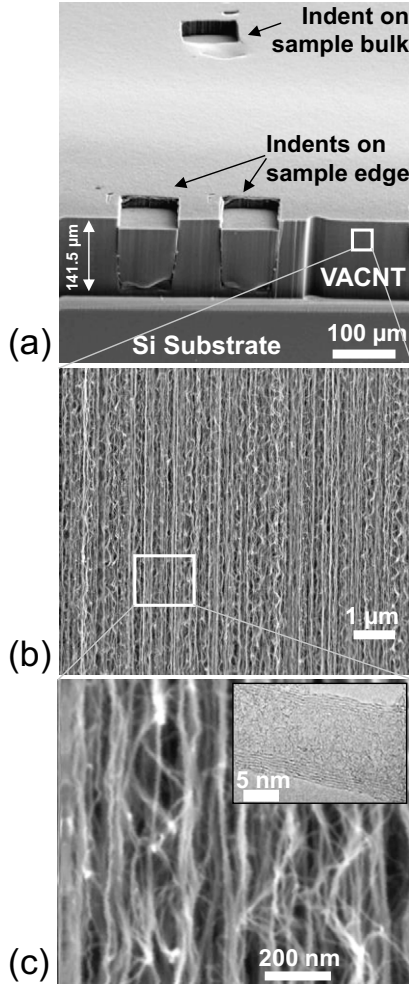

Figure 8.1. SEM images reveal the hierarchical morphology of the **(a)** 141.5 μm thick VACNT films (magnification 260X), which consist of **(b)** nominally vertical aligned CNTs visible at a lower magnification of 30kX, and **(c)** a complex intertwined network seen at higher magnifications of 240kX. SEM pictures are taken at a 60 deg tilt angle. (c inset) Individual multiwalled CNTs of outer diameter 8.8±2.1 nm (average ± standard deviation) are visible in the TEM image. (Pathak et al. 2013) reproduced with permission.

distinct organizational details across multiple length scales. Thus, while the VACNT appears as a continuous film at lower magnifications of 260X (Fig. 8.1a), the nominally vertical alignment of CNTs growing perpendicularly to the support substrate in the VACNT bundle becomes visible at a higher magnification of 30,000X (Fig. 8.1b). Increased magnification of 240,000X reveals significant intertwining in the long, curved lengths of individual CNTs, revealing the isotropic CNT network (Deshpande et al. 2000, Hutchens et al. 2010, Hutchens et al. 2011). As a result, in their as-grown states certain segments of the CNT forest appear to be pre-buckled/pre-bent, and the favourable contact energy between the tubes (van der Waals) is thought to balance the bending strain energy of their arrangement, resulting in a stable low energy configuration (Mesarovic et al. 2007). At still higher magnifications (nanometre length scales, see TEM image in Fig. 8.1c inset) – individual, discrete CNTs dominate the mechanical performance with details like CNT diameter, number of walls *etc.* governing their deformation. Such hierarchy in the VACNT microstructure governs its overall mechanical behaviour, which is a result of not only the properties of individual CNTs, but also of their complex mutual interactions and distribution throughout the array.

The method by which these structures are synthesized is the primary factor affecting their complex, hierarchical morphology. This microstructure, in turn, affects their mechanical behaviour, in particular the modulus, buckling strength, and recoverability. Synthesis techniques for VACNTs can be divided into two main categories: the Chemical Vapour Deposition (CVD) synthesis method, and the Carbide-Derived Carbon (CDC) synthesis method – which relate to the top-down vs. bottom-up growth processes respectively. In the CVD process, the VACNT film is coated onto an existing substrate. This is accomplished by depositing a thin layer of catalyst (e.g., Fe) on the substrate (typically Si or Quartz) and flowing a carbon source (e.g., ethylene) over the substrate at atmospheric pressure and temperatures typically around 750ºC. In the CDC method (Presser et al. 2011), on the other hand, carbon is formed by selective extraction of the metal or metalloid atoms in the carbide (e.g., silicon carbide) at high temperatures (>1600ºC), transforming the carbide structure into pure carbon. Since the CNT layer is formed by inward growth, this usually retains the original shape and volume of the precursor.

VACNTs grown by these different techniques demonstrate very different structure and mechanical properties. Even within materials grown via CVD, control of the growth conditions, such as the atmosphere, catalyst activity, and pressure, are known to significantly affect the repeatability of the VACNT's morphology and hence the consistency of mechanical properties (McCarter et al. 2006). For example, using 'floating' *vs.* 'fixed' catalysts Yaglioglu et al. (2012) in the CVD syntheses (Kumar et al. 2010) have been shown to result in vastly different VACNT morphologies. Differences in the growth processes used are revealed in the widely varying VACNT information reported in literature, as seen in the large range in

properties in Table 8.1. This is not to mention variations in tube diameter (from 2-3 nm (Pathak et al. 2009), to 20-50 nm (Hutchens et al. 2010), to greater than 100 nm (Qi et al. 2003)), number of walls in the CNT structure, and degree of tube alignment; properties which are sometimes neither measured nor reported. Further, the different stages of the CNT growth process can result in a height dependent inhomogeneity (Bedewy et al. 2009). This manifests as a gradient in both the density and the alignment of the tubes within the same VACNT structure. As discussed later in this entry, such a structure gradient may lead to a corresponding strength and stiffness gradient along the VACNT height. As an extreme example of the microstructure-property relationship, CDC-VACNTs are known to have a considerably higher average density (roughly 10 times higher than typical VACNTs), due to the conformal transformation of the carbide into carbon. This in turn leads to significantly larger values for the elastic modulus and yield stress in CDC-VACNTs (Pathak et al. 2009) (see Table 8.1). These promising characteristics, however, are unavailable for applications requiring macroscopic films as currently only VACNTs grown via CVD can reach macroscopic heights (~mm). Growth of CDC-VACNTs remains limited to only a few micrometres in height. Only CVD-VACNTs when used in combination with conformal coating methods, where the CNTs are coated with nanoscale coatings of ceramics like Al_2O_3 (Brieland-Shoultz et al. 2014), amorphous SiC (Poelma et al. 2014), etc. (Table 8.1) are able to reach a similar level of mechanical performances as compared to the CDC-VACNTs.

Table 8.1: Summary of Reported VACNT Elastic Modulus and Yield Strength Values. White rows denote values for CVD synthesized VACNTs, while grey rows are for CDC-VACNTs.

VACNT details (Density, porosity etc.)	Measurement Method	Modulus	Yield/ Buckling Strength	Reference
CVD-VACNTs				
87% porosity	compression	50 MPa	12 MPa	(Cao et al. 2005)
/	compression	< 2 MPa	/	(Suhr et al. 2007)
10^{10} tubes/cm^2 [a]	compression	0.22-0.25 MPa	/	(Tong et al. 2008)
97% porosity	compression	818 MPa	14.1 MPa	(Deck et al. 2007)
0.08 g/cm^3	compression	177±11 MPa	2.69±0.12 MPa	(Pathak et al. 2012)
/	compression	9-31 MPa	0.15 – 0.3 MPa	(Pathak et al. 2013)

0.008 g/cm^3 (fixed catalyst, argon anneal)	compression	1.86 MPa (range 1.3-3.26)	0.021 MPa	(Yaglioglu et al. 2012)
0.015 g/cm^3 (fixed catalyst, hydrogen anneal)		7.44 MPa (range 5.2-13.04)	0.117 MPa	
0.2 g/cm^3 (floating catalyst)		138.5 MPa	9.997 MPa	
0.018 g/cm^3	compression	/	0.12 MPa	(Bradford et al. 2011)
0.114 g/cm^3 (After post-growth CVD treatment)			5.5 MPa (After post-growth CVD treatment)	
0.12 g/cm^3	compression	0.55 MPa (parallel to the nanotube axis) 1.09 MPa (normal to CNT axis)	/	(Ci et al. 2008)
3×10^{10} / cm^2 (number density)	compression	14 MPa	compressive strength (0.8 MPa to 0.16 GPa)	(Brieland-Shoultz et al. 2014)
1 g/cm^3 (after Al$_2$O$_3$ coating)		20 GPa (after Al$_2$O$_3$ coating)		
10^{10} / cm^2 (number density)	compression	200 MPa	compressive strength <1 MPa (uncoated VACNTs)	(Poelma et al. 2014)
		125 GPa (after amorphous SiC coating)	1.8 GPa (after amorphous SiC coating)	
/	nanoindentation – Berkovich uniaxial compression	15 MPa	0.2-4.3 MPa	(Zbib et al. 2008)

Table 8.1 continued from previous page

0.08 g/cm^3	Flat punch indentation	120-175 MPa	1.49-1.75 MPa	(Pathak et al. 2013)
0.13 gm/cm^3 0.06 gm/cm^3	Flat punch indentation	7-33 MPa 100-350 MPa	0.44±0.04 MPa 0.9 MPa	(Pathak et al. 2013)
/	nanoindenta-tion – Berkovich	58 MPa	/	(Zhang et al. 2010)
/	nanoindenta-tion - Berkovich	50±25 MPa	/	(Qiu et al. 2011)
/	DMA(Dynamic Mechanical Analysis)	~ 50 MPa	/	(Mesarovic et al. 2007)
0.009 g/cm^3	DMA	~ 1 MPa	/	(Xu et al. 2010)
CDC-VACNTs				
0.95 g/cm^3	compression	30 GPa	800 MPa	(Pathak et al. 2015)
0.95 g/cm^3	nanoindenta-tion – Spherical	18-20 GPa	90-590 MPa	(Pathak et al. 2009)

Figure 8.2 highlights four literature examples of the differences in the mechanical response of various CVD-VACNT micro-pillars subjected to compression. Note in particular the higher stiffness and strength of the VACNTs grown using the floating catalyst technique in Fig 8.2a, (Cao et al. 2005) as compared to the ones grown using the fixed catalyst method (Figs. 8.2b, (Yaglioglu et al. 2012) 8.2c (Pathak et al. 2012) and 8.2d (Hutchens et al. 2010)). Other differences between these nominally identical VACNT samples are the ability of some of them to recover almost completely after large compressions (Figs. 8.2a and c) (Cao et al. 2005, Pathak et al. 2012) while others deform permanently even at modest strains (Figs. 8.2b and d) (Yaglioglu 2007, Zbib et al. 2008, Hutchens et al. 2010, Zhang et al. 2010, Cao et al. 2011).

Figure 8.2 also demonstrates the similarities in the deformation characteristics of the various VACNT systems. All of the four VACNT systems show 3 distinct regimes in their stress-strain response – elastic, plateau and densification – similar to open-cell foams. Unlike foams however, the plateau region in the VACNTs generally has a positive slope, which can vary significantly between VACNT samples. The slopes of the plateau region were calculated to be 11, 5 and 0.6 MPa for Figs. 8.2a, c, and d, respectively. Note also that all VACNT systems shown in Fig. 8.2
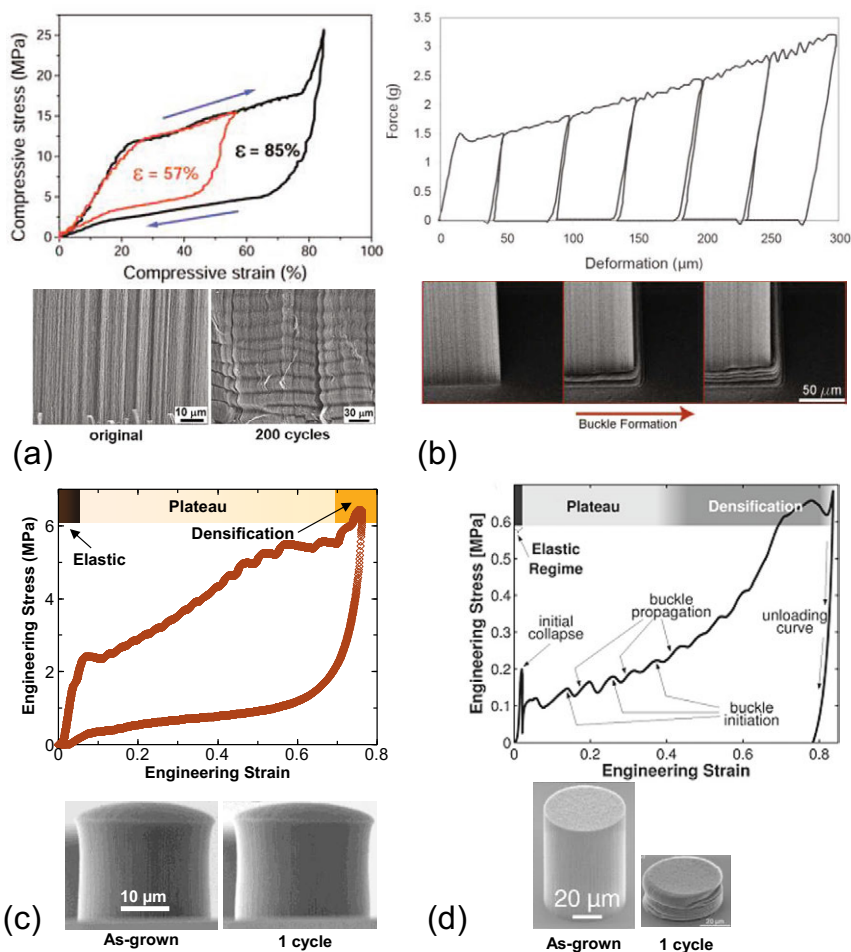
Figure 8.2. VACNT behaviour under compression for **(a)** 860 μm thick VACNT array, (reprinted from (Cao et al. 2005) with permission from AAAS), **(b)** 400 μm diameter CNT column (Yaglioglu et al. 2012) (Copyright Wiley-VCH Verlag GmbH & Co. KGaA. Reproduced with permission) **(c)** 30 μm × 30 μm (diameter × height) VACNT micro-pillar (Adapted with permission from (Pathak et al. 2012) Copyright 2012 American Chemical Society) and **(d)** 50 μm × 60 μm (diameter × height) VACNT micro-pillar (Hutchens et al. 2010) (Copyright Wiley-VCH Verlag GmbH & Co. KGaA. Reproduced with permission). All of these VACNT systems show 3 distinct regimes in their stress-strain response – elastic, plateau and densification – similar to open-cell foams. Unlike foams, the plateau region in the VACNTs generally has a strong positive slope. All VACNT systems shown here also exhibit a bottom-first sequence of buckling.

These VACNT systems differ widely in their ability to recover from large deformations. Thus while both VACNT systems in (a) and (c) show an almost complete recovery, even after multiple cycles, the VACNT systems in (b) and (d) do not exhibit any appreciable recovery.

exhibit a bottom-to-top sequence of buckling. Here the first buckle generally nucleates close to the substrate, and each subsequent lateral collapse event initiates only after the preceding one was completed, thus sequentially collapsing the entire structure. (Cao et al. 2005, Hutchens et al. 2010, Pathak et al. 2012, Yaglioglu et al. 2012) A recent report by Pathak et al. (2013) has suggested that such sequential bottom-to-top buckling and hardening in stress-strain response are observed in samples with smaller relative density at the bottom. When the density gradient was insubstantial or reversed, a different buckling sequence was observed where the bottom regions were always found to buckle last, and a flat stress plateau was obtained.

8.3.   Experimental Techniques for Studying VACNT Mechanics

Instrumented indentation, using a variety of tip geometries such as flat punch, spherical, Berkovich, and cube corner, has been the most common method for studying mechanical properties of VACNTs (Qi et al. 2003). Each geometry has its own strengths and weaknesses. While maintaining parallel contact between the indenter and the sample is a major concern for flat punch indentation, it does allow for more uniaxial-like, compressive loading. The sharper Berkovich or cube corner geometries can cause the CNTs to bend away from the indenter, testing a slightly different mode of behaviour (Qi et al. 2003, Waters et al. 2004, Waters et al. 2005). In both cases, modulus and hardness are measured from the unloading portion of the test. On the other hand, spherical indentation is advantageous in that it allows indentation stress-strain curves to be extracted from the raw load-displacement data, which enables resolution of the evolution of the mechanical response in the VACNT array: from initial elasticity, to the initiation of buckling, to post-buckling behaviour at finite strains (Pathak et al. 2009). Though indentation is a relatively simple test to perform, analyses of the results, especially non-linear elastic behaviour is difficult due to their highly localized stress fields. It is also limited in total strain.

Another testing geometry, that of uniaxial compression, eliminates these localized, applied stress fields and help reveal the existence of a localized deformation mechanism in VACNTs. In these tests, the samples are either large (~1 mm tall) bulk films and compressed between two platens (Cao et al. 2005) or microscale (up to tens of microns in height) cylinders and compressed using a flat punch indenter (Hutchens et al. 2010, Yaglioglu et al. 2012).

Both indentation and compression tests can be performed *in situ*, where the load-displacement data is gathered simultaneously with micrographs in an optical or electron microscope (SEM). These tests can offer valuable insights on the morphological evolution in the VACNTs during deformation and are discussed in detail in the next sections.

8.4. Compression Response under Large Strain

The deformation of VACNTs is governed by their hierarchical microstructure, collective inter-tube interactions, and inherent property gradient. Taken as a whole, their highly porous nature gives them an overall foam-like response. The idealized stress-strain response of traditional foams under compression is characterized by three distinct loading regimes: an initial elastic loading at low strain, followed by a plateau in the stress during which the struts bend and buckle, and finally a densification regime in which the space between struts has been nearly eliminated and the material begins to approach behaviour intrinsic to the struts themselves. For such a response, it is the intermediate plateau regime that is responsible for the bulk of energy absorption in the material, since the area under this region of the stress-strain curve, corresponding to the work done on the material, is largest. This foam-like response of a bulk VACNT film is apparent in the three distinctly differently sloped regions of the stress-strain responses shown in Fig 8.2. Locally, however, the response of VACNTs is quite unlike that of traditional foams. In VACNTs, the accommodation of strain during uniaxial compression is accomplished entirely through the formation of folds or buckles of small regions of the structure while the remaining portion remains nearly undeformed. This is in contrast to traditional foams, where cell-edge bending and cell collapse are primarily responsible for the elastic-plastic foam response (Gibson et al. 1999, Gibson 2000).The superposition of an overall foam-like response with localized strain accommodation is the key characteristic of VACNT deformation.

Experimental characterization of this buckle formation yields several interesting qualitative results. In their early study, Cao et al. (2005) compressed relatively large structures (area: 0.5-2 cm^2, height: 860 µm – 1.2 mm) and observed that the buckles formed near the bottom of the structure (the end from which the CNTs grow perpendicularly to the substrate) are more deformed that those that formed near the top (Fig. 8.2a). Motivated by this observation, they hypothesized that the bottom buckles form first. A reversal of the loading direction, by flipping the sample upside down, resulted in the same deformed morphology, with the tightest buckles forming at what was the end of the sample attached to the growth substrate. These observations point to the idea of an inherent, axial property gradient being responsible for the sequential nature of the buckling. Note that each individual buckle is on the order of 12-25 µm in size (depending on sample height) so that several tens of buckles form during deformation. The sequential, localized buckling phenomenon was later observed in much smaller samples by other researchers (Figs. 8.2 b-d) illustrating the universality of this response in VACNTs. Buckles in these microscopic studies were 12 µm (Zbib et al. 2008) and 7 µm (Hutchens et al. 2010) in wavelength (measured from the unbuckled conformation) for cylindrical samples with diameters of 30-300 µm (Zbib et al. 2008) and 50 µm (Hutchens et al. 2010),
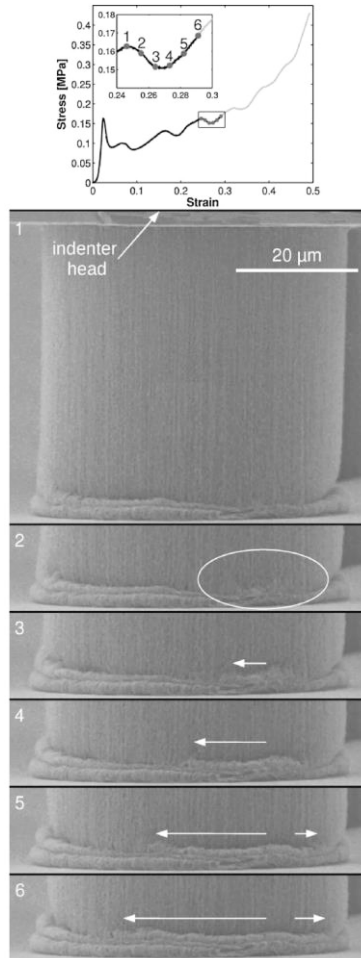
Figure 8.3. *In situ* video micrographs and accompanying nominal stress-strain data illustrating bottom-first buckling and buckle initiation and propagation events. (Hutchens et al. 2010) (Copyright Wiley-VCH Verlag GmbH & Co. KGaA. Reproduced with permission).

respectively. The bottom-first buckling mechanism was visually verified by Hutchens et al. (2010) through *in situ* experiments that further revealed the mechanism by which a single, localized buckle evolves. As shown in their study, each individual buckle does not form all at once, but rather nucleates at one point and then propagates laterally across the cylindrical sample until completion (Hutchens et al. 2010). In addition, each subsequent buckle begins only after the previous buckle has completely formed, i.e., the crease had spread across the entire cylinder (Cao et

al. 2005, Hutchens et al. 2010, Pathak et al. 2012, Yaglioglu et al. 2012). Figure 8.3 illustrates the evolution and localization of deformation for a uniaxially loaded VACNT cylinder. Cross correlation of the *in situ* images with the accompanying stress-strain data reveals that the localized buckle formation and propagation cor respond to undulations in the nominal stress-strain curve. Specifically, softening corresponds to the first appearance of the buckle and the subsequent hardening coincides with the lateral propagation of the buckle. This localized response over-lays the aforementioned overall foam-like behaviour seen in these materials.

Notable differences between the classic foam-like stress-strain behaviour and the overall response of VACNTs in uniaxial compression studies of VACNT structures have also been observed in both macroscopic (Cao et al. 2005, Suhr et al. 2007, Tong et al. 2008) and microscopic (Zbib et al. 2008, Hutchens et al. 2010) samples. First, the plateau regime is highly sloped. In typical foams, a sloped plateau indi-cates some homogeneous variation in strut buckling stress due either to random strut alignment, a distribution of strut sizes (aspect ratio, diameter, etc.), or both. While both kinds of inhomogeneity's exist in VACNTs, the plateau regime is too highly sloped to be explained by these small fluctuations. Moreover the non-local nature of the buckling points to an alternate cause. In fact, the sloped plateau regime is sug-gestive of the presence of an axial property gradient in VACNTs. As discussed previously, a gradient in tube density arises in VACNTs as a result of the CVD growth process. This gradient can be such that there is a lower tube density at the bottom of the structure (i.e., the point at which the substrate attaches) than the top. It follows that such a tube density gradient would result in a corresponding strength and stiffness gradient. This property gradient is evident in the stress-strain responses seen in Figs. 8.2 and 8.3 in the progressive increase in peak stress values for undu-lations in the plateau region. Throughout this plateau, buckles are known to form sequentially, bottom-to-top, and therefore each subsequent buckle forms at a higher (and more dense) location within the cylinder than the previous buckle, requiring a larger stress in order to form a new fold.

A recent study by Pathak et al. (2013) has reported a different buckling sequence in VACNTs. In addition to the commonly reported bottom-to-top buckling pattern (where the bottom buckle forms first), these authors also observed VACNT samples where the bottom buckle was instead the *last* buckle to form (Fig. 8.4c). These experiments were performed on two sets of VACNT micropillars, both grown by the same chemical vapour deposition (CVD) synthesis on the same Si substrate but located on different regions of the substrate. *In-situ* uniaxial compression experi-ments conveyed that the sequence in the localized folds formation was unique for each sample type (Figs. 8.4 b and c). In the first set (Fig. 8.4b) the first buckling-like instability, which corresponded to the transition from elastic loading to plateau in the stress-strain data, always formed at the bottom of the sample. After initiation, the fold propagated laterally until it fully spanned the pillar width. Bottom-to-top
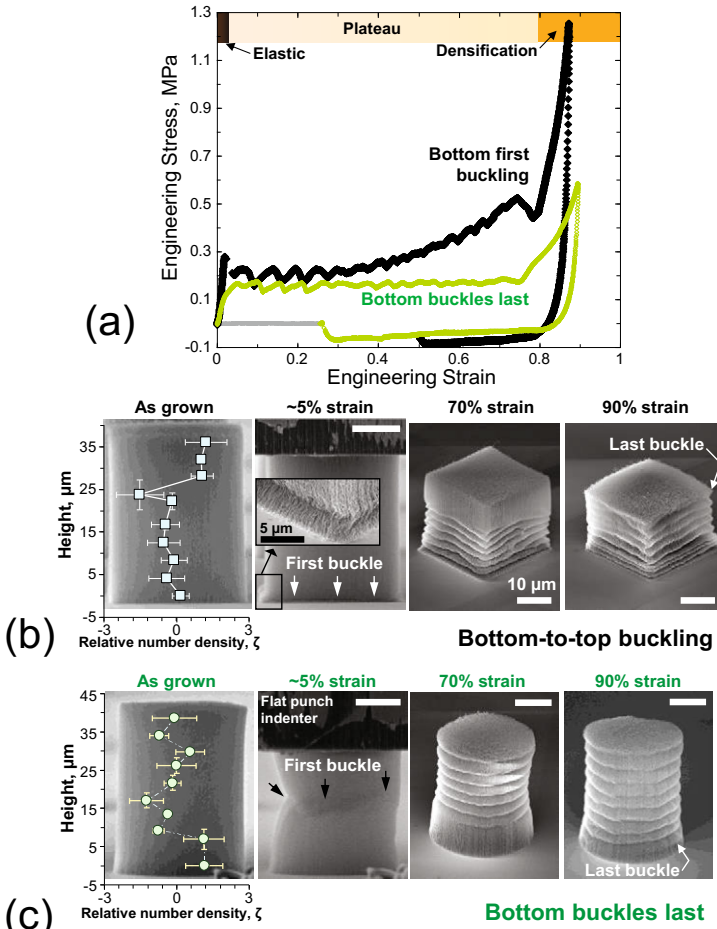
Figure 8.4. **(a)** Comparison of the stress-strain responses of two VACNT pillar systems grown on the same substrate; one showing the commonly reported bottom-to-top buckling sequence where the bottom buckle is the first one to form **(b)**, vs. the ones where the bottom buckle is the last buckle to form **(c)**. (b) and (c) also show the relationship between the relative tube number density ζ and the sequence of buckle-formation in these pillars. (Adapted with permission from (Pathak et al. 2013) Copyright 2013 American Chemical Society)

buckling occurred in succession, with each subsequent buckle initiating only after the previous one, located below it, had completed, similar to the observations in Cao et al. (2005), Hutchens et al. (2010). Unloading from maximum compression of ~70% strain left the top third of the pillar relatively undeformed (Fig. 8.4b, third panel from left), and the buckle closest to the top always formed last (Fig. 8.4b,

right-most panel). In contrast, post-compression SEM images of the second set of VACNT pillars, unloaded from the same maximum strain of 70%, showed that it was the *bottom* third of the pillar that remained relatively undeformed (Fig. 8.4c, third panel from left). The first instability in these pillars always formed somewhere at their mid-height (Fig. 8.4c, second panel from left), and the buckle closest to the substrate always formed last (Fig. 8.4c right-most panel).

The authors in Pathak et al. (2013) have suggested that the substantial differences in the deformation responses between the two pillar types shown in Fig. 8.4 were likely caused by their differing microstructural features and density gradients (the shapes of VACNT pillar cross-sections – square *vs.* circular – did not appear to influence their deformation characteristics). In order to capture the density gradients in these two pillar types the authors used edge detection analysis of systematically obtained SEM images to calculate the average relative number density, ζ, of tubes in each SEM image. Image analysis revealed that the two types of pillars exhibited opposite trends in relative density, which can be used to predict the location of initial buckling instability in a VACNT matrix (Figs. 8.4b and c). For example, it is reasonable to expect the first folding/buckling event during compressions of VACNTs to originate close to the substrate because of its rigid constraint (Zbib et al. 2008). Pillars showing a bottom-to-top buckling sequence corroborated this notion (Fig. 8.4b). These VACNT pillars had highest ζ in the top 10 μm, and their density profiles resembled a step function, where $\zeta \approx 1$ for all locations above the height of ~23 μm, and $\zeta \leq 0$ at all locales below. In contrast, the incipient instability in pillars where the bottom buckles formed last occurred somewhere in the middle of pillar height, at the locales with the lowest relative CNT density (Fig. 8.4c). Maximum ζ in these pillars was located in the bottom ~10 μm, close to the substrate, while the minimum ζ was in the midsection of the pillars. It appears that the lower relative density trumps the constraining effects of the substrate in driving the location of the buckling instability in these pillars. The last buckles in both sets of pillars occurred in the regions with the highest relative CNT densities: near the top in the samples showing bottom-to-top buckling sequence and at the base in the ones where the bottom buckles formed last.

In addition these two pillar types also show some key differences in their stress-strain response (Fig. 8.4a). The stress plateau in the pillars showing bottom-to-top buckling had two separate slopes: a relatively flat section up to 30% strain and a steeper region, with the slope of 0.65 MPa up to unloading at 75% strain. In contrast the pillar set where the bottom buckles formed last had a nearly flat plateau (slope ~ 0.02 MPa) up to a strain of 75%. There was also a noticeable difference in the amount of recovery between the two sample types when unloaded from post-densification regime: pillars showing bottom-to-top buckling ($R \approx$ 57.9±0.9 %) showed an almost 45% higher recovery than those where the bottom buckles formed last ($R \approx$ 39.8±3.9 %).

It has been suggested that such differences in the compressive responses of VACNTs can be predicted based on their local variations in density along the VACNT sample heights. Such property dependence was initially modelled by Hutchens et al. (2010) in a viscoplastic finite element framework which showed a direct correspondence between the presence and extent of an applied property gradient and the amount of hardening within the plateau. Details of this and other efforts to capture VACNT deformation mechanisms through modelling are summarized in the next section.

8.5.   Modelling of VACNT Deformation

Only a few preliminary models exist to describe the mechanical deformation of VACNTs. Motivated by both the morphology of the VACNTs (a series of nominally vertical struts) as well as the observed buckling behaviour, many researchers utilize an Euler buckling framework to mechanistically describe their findings. In Euler buckling, an ideal column (perfectly straight, homogeneous, and free from initial stress) is determined to buckle when the applied load reaches some critical value that causes the column to be in a state of unstable equilibrium. Up to the point of buckling, the column is assumed to be perfectly elastic. Scaling calculations by Cao et al. (2005) utilize this critical stress to estimate the transition stress value for departure from linear elastic behaviour, i.e., the buckling stress, given a reasonable estimate of the tube number density. Similarly, Mesarovic et al. (2007) included an additional intertube contact energy to account for favourable van der Waals interactions between tubes in their energetic treatment of VACNTs. Another Euler based model by Zbib et al. (2008), motivated by the formation of buckles they observed, proposes piece-wise buckling that assumes the top of the pillar deforms via simple shear while the bottom undergoes collapse. Using this framework, they predict the buckling stress increases asymptotically with decreasing pillar height (for similar aspect ratio pillars). Notably, however, none of these models make predictions concerning the length-scale of the buckles formed or their dependence on material parameters such as density, stiffness, tube alignment, or size as the parameter space is difficult to grow in these materials.

Another subset of mechanical analyses utilizes an alternating hardening-softening-hardening local constitutive relation, and are the only theories that attempt to capture material response beyond the initial buckling event. The first, a hierarchical bi-stable spring model, captures the *quantitative* stress-strain response of VACNTs in compression (Fraternali et al. 2011). A subsequent finite element viscoplastic solid with a positive-negative-positive sloped flow strength captures the *qualitative* sequential periodic buckle morphology. The bi-stable spring model consists of mesoscale elements characterized by elastic-plateau-densification and, most importantly, hysteresis in the unloading curve. These mesoscale elements were

shown to be the limiting case of infinitely many bi-stable spring elements in series. Briefly, a bi-stable spring consists of two thermodynamically stable elastic loading sections separated by an unstable, negative stiffness region of the stress-strain curve across which the material snaps, similarly to a phase transition. When placed in series, these mesoscale elements capture the hysteretic unloading response seen by Cao et al. (2005) very closely. Thus, this model can be utilized to characterize the energy dissipation in VACNTs. In a similar vein, Hutchens et al. (2011) postulate a
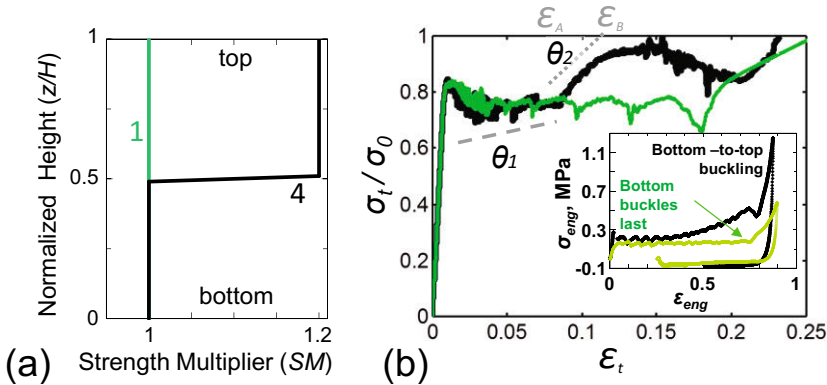

Figure 8.5. (a) Two variations of the *SM* (strength multiplier) function used for simulations: Case 1: constant *SM* function (green curve) vs. Case 4 (step variation of the *SM* function over the pillar height, black curve). **(b)** Corresponding normalized stress-strain curves for these two cases. Note that the plateau region in Case 4 can be further subdivided by two distinct slopes, $\theta1$ and $\theta2$. (b Inset) Experimental uniaxial stress-strain responses of the two VACNT pillars shown earlier in Fig. 8.4 showing the similarity in their responses as compared to the two simulation cases in (a). (Adapted with permission from (Pathak et al. 2013) Copyright 2013 American Chemical Society)

positive-negative-positive stress-strain relation reminiscent of a bi-stable spring, but rather than being elastic, it is used as a plastic flow-strength function governing the local deformation of an element post-elastic loading. The latter analyses find that this constitutive relation is capable of producing sequential, periodic buckles in an axisymmetric, circular cylindrical mesh with fixed boundary conditions at the base, identical to those in VACNTs. In addition, an axial gradient in the strength is not necessary to initiate bottom-first buckling, as seen in experiments; rather, the fixed boundary conditions are sufficient. However, a reversal of buckle initiation, top-to-bottom, can be achieved for a sufficient inverse axial gradient (having lower strength at the top of the pillar than the bottom). Both of these analyses capture essential elements of VACNT deformation, but do so for two very different sets of experimental observations: recoverable deformation, and plastic deformation.

An example of the approach proposed by Hutchens et al. (2011) is shown in Fig. 8.5. Here the same model was utilized to predict the stress and strain responses of the two VACNT pillar types shown earlier in Fig. 8.4, assuming the stiffness of VACNTs to be linearly related to its density, $E \sim \zeta$. The mechanical property gradient was represented by a strength multiplier, *SM*, which is a multiplier giving the spatial variations of *E* (Young's modulus) and σ_0 where $SM=E/E_{bottom}$ and similarly for σ_0. Two particular cases are of interest (which matches the experiments most closely): Case 1 – *SM* is constant throughout the pillar height, and Case 4 – *SM* has a step-increase at the midpoint of the pillar height *i.e.* at $z/H=0.5$, where *z* is the coordinate along the pillar height. Strength gradients over the height in terms of *SM* for the two cases considered are shown in Fig. 8.5a, and normalized stress-strain data are shown in Fig. 8.5b. Of special note is the similarity between the experimental and simulated stress *vs.* strain relationships (Fig. 8.5b inset) in these two cases – such as the flat plateau region for a constant *SM* function (Case 1), similar to the experimental case where the bottom buckles form last, as compared to the two different hardening slopes observed for the step function in *SM* (Case 4), similar to the experimental case of bottom-to-top buckling.

8.6.   Large Displacement Indentations in VACNTs

In addition to uniaxial compression, large displacement (in the range of tens of micrometres) indentations using flat punch indenters (which offer a constant contact area with the sample) offers an alternative approach to analysing VACNT deformation under a different loading and boundary condition. These tests, conducted by a variety of researchers (Lu et al. 2012, Pour Shahid Saeed Abadi et al. 2012, Pathak et al. 2013, Pathak et al. 2013), help in comparing the influence of the boundary conditions posed by the presence or absence of the external matrix.

A comparison between the indentation responses at the sample-edge vs. the one in the sample interior was provided by Pathak et al. (2013) for flat punch indentations of a ~142-µm thick VACNT film on a Si substrate grown using an atmospheric pressure CVD synthesis technique (Fig. 8.6). The following salient points are of note from this figure. Firstly this plot indicates that while the curves are similar in shape, the on-edge regions deform at significantly lower loads than in-bulk locations at equivalent indentation depths. This result is not surprising due to the less restrictive boundary conditions in the on-edge setup. Secondly, in both cases the load first increases steeply up to an instability manifested by a large displacement burst of ~20 µm, after which the indenter tip is unloaded (Fig. 8.6a). SEM images obtained immediately after this burst reveal that a portion of VACNT film sheared off nearly perfectly vertically along the edges of the indenter tip (Fig. 8.6c). In the sheared off region the deformation appears to be highly localized, occurring only at the shear offset regions and at the buckles formed at the bottom of the sample. The remaining
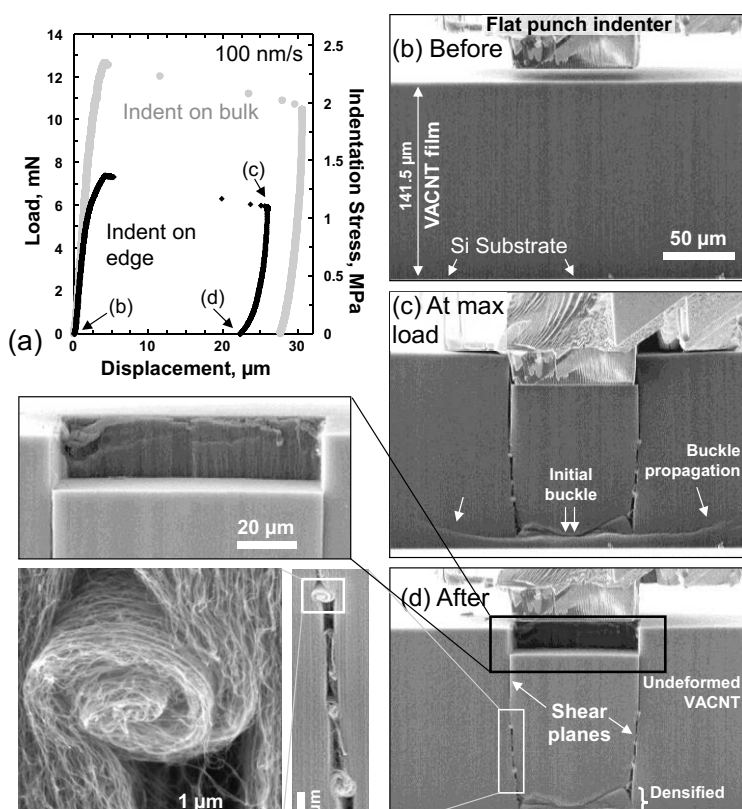
Figure 8.6. Large displacement indentations in VACNTs. **(a)** Comparative indentation load (and stress)-displacement curves at 100nm/s loading rate of *in-situ* SEM indentation tests conducted on the sample edge vs. in the interior of the sample using a 60 µm × 80 µm rectangular flat punch indenter . **(b, c and d)** For the indent on edge, the indentation process was recorded as a video file from which individual picture frames were extracted corresponding to a particular event during the loading/unloading cycle (as indicated on the load–displacement graph).

The double arrows in (c) mark the initiation of the first buckle at a load of around 6 mN. The wide lateral buckle marked by single arrows are formed after the first buckle, and increase in size with loading. (d) Upon unloading these lateral buckles disappear. **(d inset top)** The large displacement burst results in a vertical shear of the VACNT structure along the indenter edges. Note the clean edge of the shear wall. **(d bottom insets)** The shear appears to have been carried by a series of CNT 'micro-rollers' which act as effective lubricants protecting the rest of the VACNT structure from further damage. (Pathak et al. 2013) reproduced with permission.

portions of the VACNT film appear completely unaffected (Fig. 8.6d top inset). Thirdly, the shear appears to have been carried by a series of tangled CNTs, or 'micro-rollers' seen in the magnified inset images in Fig. 8.6d, whereby original-ly-vertical strands of several entangled CNT collectively coiled themselves into helical structures. The authors have speculated that these micro-rollers provide a low-friction path during the shear process. Finally unloading the indenter tip results in minimal recovery.

The shear event and the formation of the CNT micro-rollers are unique charac-teristics seen only in the intertwined VACNT systems. Neither foams (Sudheer Kumar et al. 2003, Flores-Johnson et al. 2010), where the deformation is confined only to regions directly beneath the indenter, nor non-interacting VACNTs (Pantano et al. 2004), where such shear would propagate without any micro-roller formation, show the unique features seen in Fig. 8.6.

Some of these phenomena can be understood in terms of the differences in boundary conditions between the two loading configurations – indentation (Pathak et al. 2013) vs. compression (Pathak et al. 2012) (Fig. 8.7), in combination with the overall similarity of the VACNT deformation to that of open-cell foam materials (Gibson et al. 1999). The characteristics of flat-punch indentations into VACNT films closely resembles those reported for metallic (Andrews et al. 1999, Sudheer Kumar et al. 2003) and polymeric foams (Flores-Johnson et al. 2010) (Gibson et al. 1999). In the spirit of foam-like deformation, the indentation zone for VACNTs is confined to the region directly beneath the indenter, while the surrounding regions are unaffected (see Fig. 8.6). The lack of lateral spread in the deformed region is typical for foams, whereby it can be attributed to the non-existent Poisson's ratio (Gibson et al. 1999, Sudheer Kumar et al. 2003, Zbib et al. 2008). This is diamet-rically opposite to monolithic materials, where the plastic zone underneath the indenter tip is typically represented by a continuous hemispherical plastic zone (Fleck et al. 1992). Another common characteristic between indentation into con-ventional foams and VACNTs is the appearance of a so-called 'tear line' (Sudheer Kumar et al. 2003, Flores-Johnson et al. 2010) along the corner of the flat punch indenter where the shear force is largest. The depth of this shear line in a foam generally depends on its strength (Sudheer Kumar et al. 2003, Flores-Johnson et al. 2010). Unlike foams, however, the constituents of the VACNT system – the indi-vidual CNTs themselves – are nominally vertically aligned with respect to the indenter tip (Fig. 8.1), and thus the vertical plane is expected to be the plane of lowest shear strength in the VACNT matrix. Once the critical shear stress is attained during loading, the shear-off proceeds catastrophically along this vertical plane through the thickness of the VACNT film down to the underlying substrate. This results in highly localized deformation along the shear plane, with no notable per-turbation in other regions. Subsequent loading initiates folding or buckling of the material close to the substrate but not in the sheared-off block.

On the contrary, under uniaxial compression the shear stresses acting on the VACNT matrix are negligible. Instead, the applied compressive strain is accommodated entirely via the formation of lateral folds or buckles along the length of the bundle, while the remaining portion remains virtually unscathed (Hutchens et al. 2010, Pathak et al. 2012). Thus, the first instability shown in the compression stress-strain response in Fig. 8.7a is related to the onset of the first buckle formation in the VACNT matrix. Further loading beyond yield results in the compression of the collapsed buckles.

A comparison of the instability stresses between compression (buckling, 2.69±0.1 MPa) and indentation (shear, 1.75±0.3 MPa) on the CVD VACNT samples indicate
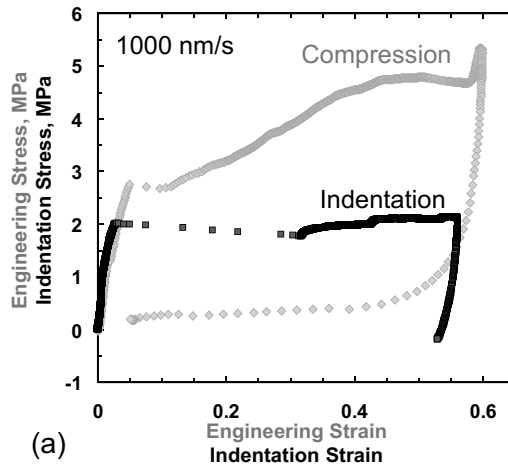
(b) 1000nm/s	Indentation	Compression
Instability stress	1.75±0.3 MPa (shear)	2.69±0.1 MPa (buckling)
Recovery @ ε=0.5	4.3±0.3 %	95.7±2.8 %
Loss Coefficient @ ε=0.5	0.005±0.001	0.05±0.01
Modulus @ ε=0.5	173.7±2 MPa	176.9±11 MPa

Figure 8.7. (a) Comparative stress-strain curves of VACNT in indentation and compression **(b)** Table comparing the measured values from indentation (Pathak et al. 2013) vs. compression (Pathak et al. 2012). (Pathak et al. 2013) reproduced with permission.

that the instability stress in indentation is 40% lower than that of compression (Fig. 8.7b). Interestingly, this observation is opposite to that of traditional indentation tests into monolithic materials, where yield in indentation typically requires 1-3

times higher stresses than for the uniaxial case for most solid (Johnson 1987) and porous (Fleck et al. 1992) as well as foam (Gibson et al. 1999, Andrews et al. 2001, Sudheer Kumar et al. 2003) materials. The two distinct modes of deformation in VACNTs – shear under indentation, and buckling in compression – are likely responsible for this apparent reversal in their instability stress values, i.e. during indentation the APCVD VACNT film reaches its critical shear stress before it can buckle.

8.7. Recoverability from Large Strains

A marked difference in material behaviour among different VACNT arrays is the ability (or lack thereof) to recover from large deformations; with some exhibiting superior creep recovery, seeing less than 15% deformation after thousands of cycles of strain to 85% (Cao et al. 2005, Suhr et al. 2007, Xu et al. 2010, Xu et al. 2011, Pathak et al. 2012), while others deform permanently even at modest strains (Yaglioglu 2007, Zbib et al. 2008, Hutchens et al. 2010, Zhang et al. 2010, Cao et al. 2011) (see Fig. 8.2). Energy can be dissipated in the former as they behave like viscoelastic rubbers, discussed in a later section. Energy can be absorbed in the latter. Both appear to deform via the same structural mechanism intrinsic to the complex microstructure of these systems. It is still largely unclear what is responsible for a VACNT material displaying plastic versus viscoelastic behaviour.

A number of experimental studies have identified a list of potential candidates that affect the recoverability of VACNTs. Pathak et al. (2013) have shown that both the experimental loading and boundary conditions as well the VACNT morphology have a marked effect on VACNT recoverability (Fig. 8.7). These authors have reported a large difference in recoverability of the VACNT matrix in indentation (4.3±0.3 %) vs. compression (95.7±2.8 %) conditions. This has been attributed to the different deformation modes and boundary conditions under the two loading modes. The almost complete recovery of the VACNT structure under compression in (Pathak et al. 2012) is related to the elastic un-folding of the buckles created during loading. This recoverability has been explained by the inter-tube interactions of the CNTs where the zipping and unzipping of CNTs in contact has been proposed as the primary criteria for the superior viscoelasticity and creep recovery of VACNTs (Gogotsi 2010, Xu et al. 2010, Bradford et al. 2011, Xu et al. 2011). On the contrary, recovery in indentation (Pathak et al. 2013) is inhibited by the additional constraints of the surrounding VACNT material. Thus even at lower strains (before the large shear burst) the recovery under indentation is still lower (50-80%) than that in compression. Moreover indentation experiments cause large shear forces to develop along the corners of the flat punch indenter. This causes the VACNT films to deform by an instantaneous vertical shearing of the material directly underneath the indenter tip (since the vertical plane is the plane of lowest

shear strength in the vertically aligned CNT matrix). After the displacement burst, recovery of the VACNTs in indentation is further compromised by the permanent nature of the damage caused by the shearing of a large block of the material from the matrix (Lu et al. 2012, Pathak et al. 2013).

The recoverability of VACNTs has also been shown to depend on the VACNT microstructure and morphology. In general, researchers growing CVD-VACNTs made using the 'floating' catalyst route (Andrews et al. 1999, Raney et al. 2011) have reported substantial (>90%) recovery in their samples (Cao et al. 2005, Raney et al. 2011, Raney et al. 2011, Yaglioglu et al. 2012), while the recoverability of majority of VACNTs made using the 'fixed' catalyst technique (Yaglioglu 2007, Bedewy et al. 2009) has been poor (Zbib et al. 2008, Hutchens et al. 2010, Zhang et al. 2010, Cao et al. 2011) (note: Pathak et al. (2012) is a notable exception). This effect is thought to be correlated to the thicker (>40 nm) diameter of the tubes, and a correspondingly higher density for VACNTs made using the floating catalyst route. A systematic study by Bradford et al. (2011) analysed this effect further, where it was shown that VACNTs grown using a fixed catalyst technique and exhibiting low resilience changed to an almost complete recovery after a post growth CVD treatment (Fig. 8.8a). This was attributed to an increase in the individual CNT wall thickness, which also caused increased surface roughness of the CNTs, resulting in a decrease of the van der Waals interactions.

Other aspects of the VACNT microstructure are also known to influence their mechanical properties, such as their tortuosity (or waviness) and the number of inter-tube junctions in the matrix, both of which are expected to increase with increasing CNT wall thickness and/or density of the sample (Astrom et al. 2004, Berhan et al. 2004). The effect of tortuosity on VACNT recovery has been demonstrated by Pathak et al. (2013) (Fig. 8.8b). In their work the authors synthesized two VACNT samples using the same nominal CVD growth conditions, but for different reaction times. This resulted in a taller VACNT film (Sample A in Fig. 8.8b), which in addition to having a higher density and CNT wall thickness, also showed increased tortuosity/waviness in its top portions. During flat punch indentation, sample A showed almost full recovery, while sample B (in which the CNTs have negligible tortuosity and follow relatively straighter paths) showed a much lower (~49%) recovery (Fig. 8.8b).

As discussed earlier, VACNTs subjected to large displacement flat punch indentations often exhibit a catastrophic shear-off event, which limits their recoverability. Thus the very high recovery of sample A is quite unique for VACNTs, and can be linked to its tortuous nature. The tortuosity/waviness of the CNTs in sample A is expected to cause a higher number of inter-tube contacts in its as grown state, and such interconnections are instrumental in increasing the vertical shear strength of the matrix and hence prevent any catastrophic shear off under indentation. The recovery process is also aided by the larger CNT wall thickness of sample A and the resultant

increase in the bending stiffness of the tubes. On the other hand, the more vertical alignment of the constituent CNTs in sample B results in a lower shear strength in the vertical plane of this sample, resulting in the expected catastrophic shear-off event, and hence negligible recovery (Fig. 8.8b).
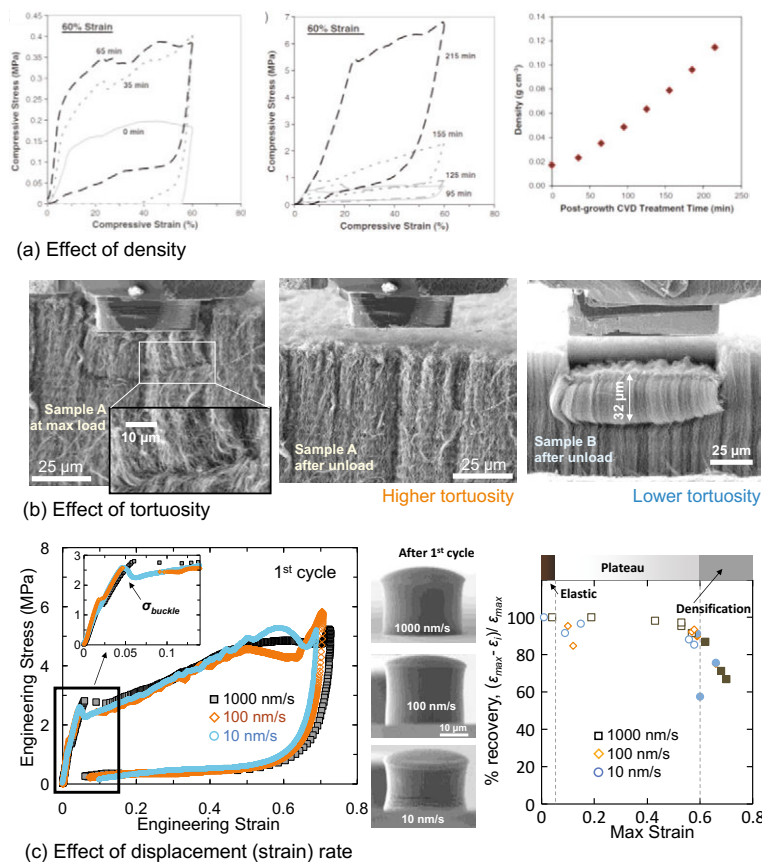

(a) Effect of density

(b) Effect of tortuosity

(c) Effect of displacement (strain) rate

Figure 8.8. Factors affecting recoverability in VACNTs. % recovery in VACNTs increases with **(a)** increasing density (Reproduced from (Bradford et al. 2011) with permission from Elsevier) **(b)** increased tortuosity of VACNTs (Reproduced from (Pathak et al. 2013) with permission from Elsevier) and **(c)** higher displacement (strain) rates (Adapted with permission from (Pathak et al. 2012) Copyright 2012 American Chemical Society).

For VACNT bundles demonstrating nearly full recovery and energy dissipation, a further factor that affects the resilience of these systems is the displacement (strain) rates at which the compression tests were conducted (Pathak et al. 2012). This is shown in Fig. 8.8c for VACNT systems grown using 'fixed' catalyst techniques for three explored strain rates: 4×10^{-2}, 4×10^{-3} and 4×10^{-4} /sec (which correspond to

displacement rates of 1000, 100 and 10 nm/s respectively). These authors found that when compressed at the fastest strain rates of 4×10^{-2}/sec, the VACNT bundles recover virtually back to their original dimensions (> 95 % recovery) while at the slowest deformation rates of 4×10^{-4}/sec, they remain permanently deformed (< 86 % recovery), as evidenced by their post-mortem morphology containing localized buckles. The resilience of the VACNT samples is further compromised when they are loaded to beyond densification threshold strains of $\varepsilon \geq 0.65$-0.7 for all strain rates.

All of this suggests a strong dependence of deformation commencement on strain rate, the basic phenomenological process for which may be understood as follows. When compressed at the lower deformation rates, the individual CNT struts re-arrange themselves by twisting, bending, *etc.*, in response to the applied compressive load, thereby coming into close contact with one another. This type of individual strut re-configuration is not unreasonable in a high-entropy deformation process (*i.e.* many different configurations are available at each time step). In addition, CNTs are inherently "sticky," experiencing an adhesive driving force due to van der Waals interactions (Ruoff et al. 1993). Therefore, in the course of compression at the slower rates, an ever-increasing number of individual struts coalesce by coming into close proximity of one another, thereby forming localized densified regions (*i.e.* buckles). Importantly, the adhesion process appears to be largely irreversible, *i.e.* the adhesion driving force overrides the stored elastic energy upon unloading. This implies that after unloading the buckles remain even while undergoing elastic recovery. This all is in contrast to the deformation at higher rates, where the entire structure recovers completely, with no evidence of buckles' presence upon unloading (see Fig. 8.8c). This behaviour is believed to stem from an insufficient interaction time between individual tubes to come in contact with one another. This results in a significantly reduced contact inter-tubular area as compared with the slowly-deformed case, and hence leads to much lower adhesion. Compression at higher rates is likely a lower-entropy process since there are fewer configurations available during each time step, and therefore less inter-tubular contact occurs, leading to the lack of localized "zipped-up" densified buckles (Gogotsi 2010, Xu et al. 2010, Bradford et al. 2011, Xu et al. 2011).

A corollary to the above hypothesis is that if different VACNT micro-pillars were allowed similar amounts of time for the reconfiguration to occur, they should exhibit similar % recovery for all loading rates. This was demonstrated in Pathak et al. (2012) by conducting two tests: one at the slowest 4×10^{-4}/sec rate, and a second one at the fast rate of 4×10^{-2}/sec where the sample was held at the max load for a long time to ensure that it spends an equivalent amount of time before unload similar to the sample deformed at the slowest rate. Both pillars showed (equally reduced) recovery values of 86%. The above results suggest that it is the time spent by the VACNTs under high strains, rather than the loading history, that determines the permanence of their deformation.

8.8.   Carbide Derived Carbons (CDC) VACNTs

While most of the previous sections in this chapter have focused on CVD-VACNTs, VACNTs prepared by the Carbide-Derived Carbon (CDC) synthesis method also deserve special mention. As discussed earlier, CDC-VACNTs refer to a bottom-up growth process, where carbon is formed by selective extraction of the metal or metalloid atoms in the carbide (e.g., silicon carbide) at high temperatures ($>1600^{\circ}$C), transforming the carbide structure into pure carbon. It has been shown (Kusunoki et al. 1997) that high temperature decomposition of SiC by the reactions SiC $\rightarrow$ Si(g) + C, SiC + 1/2O$_2$ (g) $\rightarrow$ SiO (g) + C, leads to the formation of CNTs growing normal to the carbon terminated $(000\bar{1})$ C-face of hexagonal SiC with primarily zigzag chirality (Kusunoki et al. 2002) and graphite growth on the Si terminated (0001) Si-face. These carbide-derived carbon (CDC) nanotube brushes have been shown to have a density close to 0.95 g/cm^3 (Cambaz et al. 2008), which is significantly (10 times or more) higher than in catalytic CVD growth of any kind of nanotubes. This higher density is generally thought be due to a conformal transformation of SiC into carbon. These dense CDC CNT brushes consist of small-diameter (1-3 nm outer diameter, 1-4 walled) non-catalytic CNTs with double walled CNTs being the most common, as determined from transmission electron microscopy (TEM), and a strong RBM mode in Raman spectra (Cambaz et al. 2008). Assuming an average outer diameter of 3 nm and 0.35 nm as the inter-tube distance, this would correspond to an aerial density of ~100,000 tubes per µm^{-2} for a hexagonal arrangement of CNTs, and ~89,000 tubes per µm^{-2} for a square arrangement. The actual aerial density of the CNTs packed randomly in a dense brush is likely to be somewhere in between.

The higher density of these CDC-VACNT brushes is evident in the SEM image in Fig. 8.9a inset of the CNT brush grown at 1700°C, where no apparent porosity is visible. Such dense VACNTs are ideal for indentation testing using smaller spherical indenters, something that is not possible for the wider spaced CVD-VACNTs (where the CNTs tend to simply bend away from the indenter). The use of spherical indenters is also advantageous in that, by using appropriate data analysis protocols (Kalidindi et al. 2008, Pathak et al. 2015), the extracted load-displacement data from these tests can be transformed into meaningful indentation stress-strain curves. The indentation stress-strain curves in turn enable one to follow the entire evolution of the mechanical response in the VACNT array, from initial elasticity to the initiation of buckling to post-buckling behaviour at finite plastic strains. In addition, the indentation stress-strain curves also allow one to estimate the Young's modulus and the stress at buckling in the indentation experiment. For example, using a 1 µm spherical indenter, the Young's modulus of 200 nm thick CDC-VACNT brushes was estimated to be ~17 GPa and the critical buckling stress was estimated as ~0.3 GPa at a load of 0.02 mN (Pathak et al. 2009).

The authors in Pathak et al. (2009) also used indentation stress-strain curves from different indenter radii to explore the effects of indentation zone sizes and the ma-
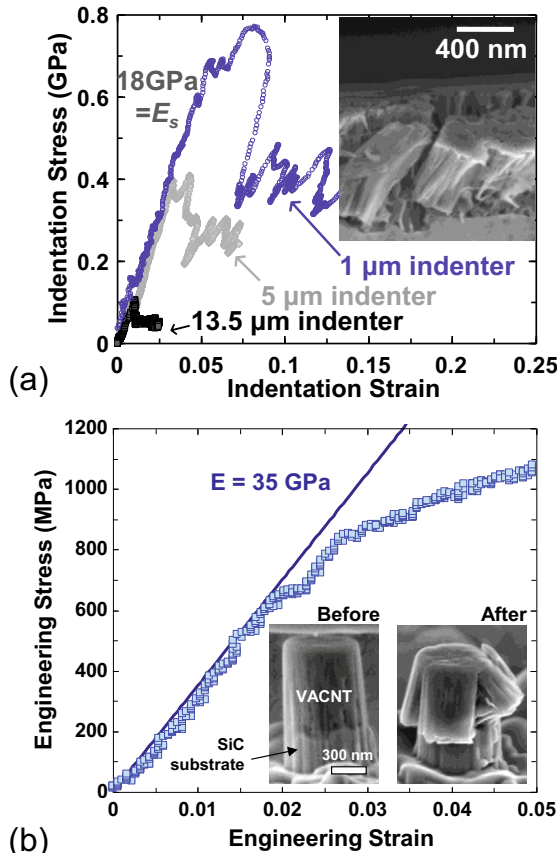

Figure 8.9. (a) Indentation stress-strain response on 1.3 μm thick CDC-VACNT brush as a function of indenter size (radius) showing an initial elastic behaviour followed by the buckling instability (Reproduced from (Pathak et al. 2009) with permission from Elsevier). **(b)** Uniaxial compression of a CDC-VACNT micro-pillar of diameter ~ 600 nm. The inset images show the VACNT micro-pillar before and after compression (Reproduced from (Pathak et al. 2015) with permission from Elsevier).

terial defect density on the VACNT buckling stress. This is shown in Fig. 8.9a where the indentation response on a thicker VACNT brush (thickness 1.2-1.4 μm, see Fig. 8.9a inset) is shown as a function of 3 different indenter radii. In general all three indenter sizes show a similar trend in the VACNT response: an initial elastic behaviour (Young's modulus ~18 GPa), followed by a sharp drop at a critical stress corresponding to CNT buckling. Note however that the values of buckling stresses

vary significantly between the three different indenters, where indentation with the smaller 1 µm indenter shows the highest buckling stress, followed by the 5 µm indenter, while buckling with the largest 13.5 µm indenter occurs at a significantly lower indentation stress.

Such differences in buckling stresses can be understood by a closer analysis of the indentation zones sizes between the 3 indenter radii used. The indentation zone sizes at buckling for the larger 13.5 µm indenter (~3.58 µm) extends well beyond the VACNT brush thickness (1.2-1.4 µm), while only a limited thickness of the VACNT brush (~ 0.39 µm) is exposed to indentation stress for the smaller 1 µm indenter. The corresponding differences in buckling stress are thus largely a consequence of the effective buckling length available in each case; with smaller indenters there is only a smaller buckling length and the material is able to withstand higher buckling stresses. Interestingly the authors in Pathak et al. (2009) also report a larger variation in the values of the buckling stress for the small 1 µm radii indenter as compared to the larger indenters. These values seem to indicate that defect density varies from one location to another in one VACNT brush. Thus the smaller volume sampled by the 1 µm indenter is more sensitive to the variation in defect density when different regions of the sample are probed, and causes a larger spread of the buckling stress values when using this indenter. The larger indenters, on the other hand, encounter a bigger volume, and hence they mostly register a combined VACNT-defect response leading to a lower buckling stress and a smaller spread in the buckling stress.

The above results have been validated by conducting compression tests on VACNT micro-pillars machined using a focused ion beam (FIB) on the same sample. This is shown in Fig. 8.9b which shows the uniaxial compression data for a ~600 nm diameter VACNT pillar. As seen from this figure, the values measured from indentation and compression tests are complementary to one another. The increase in the Young's modulus values in the micro-pillar compression tests (~30 GPa as compared to ~17-18 GPa in indentation) is due to ion-beam irradiation during the micro-machining process using FIB. This modifies the structure of the outer rim of CNTs in the VACNT pillar, which potentially results in intertube bridging between the densely packed CNTs and hence an increase in their Young's modulus (Kis et al. 2004).

These numbers suggest that these CDC-VACNT brushes perform significantly better and exhibit considerably higher mechanical properties compared to CVD VACNT turfs; CDC-VACNTs have values of Young's modulus 1-2 orders of magnitude higher (Mesarovic et al. 2007), and buckling strengths several orders of magnitude higher (Waters et al. 2004, Waters et al. 2005) compared to a CVD VACNT turf – a difference which is explained by the much higher density of the tubes per unit area in the CDC-VACNT resulting in considerably higher mechanical properties. These higher properties are of extreme importance for making selective

CNT membranes for gas or liquid filtration/separation or CNT coatings for tribological applications.

8.9. Viscoelasticity

In addition to their distinctive buckling behaviour and their ability to recover from large deformations, VACNTs have also been reported to demonstrate another case of extreme mechanical performance – a unique viscoelastic response that spans a truly wide temperature range from -196°C to 1000°C – something no other material has shown so far. Viscoelastic materials exhibit both viscous and elastic characteristics when subjected to load. Thus, a viscoelastic material is able to both dissipate energy through viscous behaviour (as in honey), while storing energy though elasticity (as in rubber band). The stress-strain response of viscoelastic materials is typified by hysteresis in the loading-unloading cycle.

Viscoelastic behaviour in a material is generally characterized in terms of its loss (E'') or storage modulus (E') (or by the ratio, known as tan $\delta = E''/E'$, of these two moduli). E'' relates to the amount energy dissipated while E' represents the stored energy in the material. The angle δ is the phase lag between the oscillatory load and displacement responses under a sine wave load. In a typical experiment, the material is loaded to a pre-determined strain and the mechanical probe is oscillated across a range of frequencies. By measuring the resultant load amplitude, displacement amplitude, and the phase lag during the test, the values of loss modulus, storage modulus, and tan δ are determined. Similarly, viscoelasticity can also be quantified by the memory or hysteresis effects during load-unload cycles under deformation, where the energy dissipated is given by the area of the hysteresis loop. These viscoelastic effects have recently been documented in the highly intertwined random networks of VACNTs. Viscoelasticity in CVD-VACNTs has been demonstrated by Hutchens et al. (2010), where both storage and loss stiffness's were studied in a frequency range from 1 to 45 Hz at different strain levels (Fig. 8.10a). Note that these stiffness values are proportional to moduli given a known Poisson's ratio which is lacking for VACNTs. The elastic response is clearly frequency independent, indicating the VACNT's elastic deformation is likely due to the same mechanism (likely tube bending) over the range of timescales tested. As shown in Fig. 8.10a, more energy is dissipated (higher values of loss stiffness's) at larger strain levels when a higher fraction of the VACNT pillar has buckled. Interestingly, for the more dense CDC-VACNTs the opposite seems to be true (Fig. 8.10b). For the highly dense CDC-VACNTs, Pathak et al. (2009) have shown a significant drop in the tan δ values of the CNTs after buckling, i.e., when the material was highly compacted. These observations indicate that while an increase in density can significantly increase the viscoelastic behaviour of CNTs, there appears to be a cut-off beyond which the contacting CNTs became increasingly bundled resulting in a

decrease in their ability to dissipate energy.

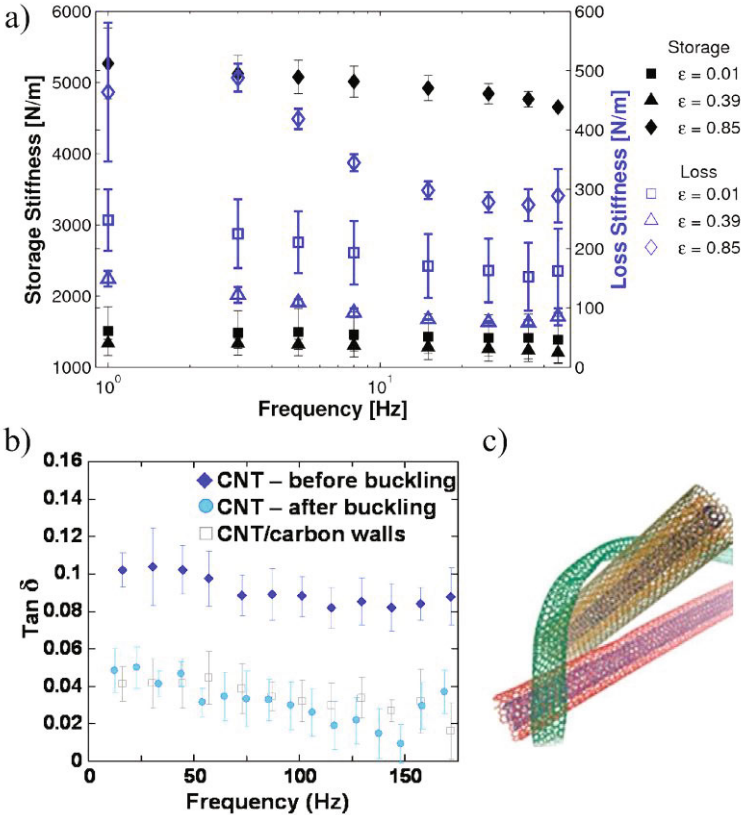A recent report by Xu et al. (2010) also suggests a rubber like viscoelastic be-

Figure 8.10. Visco-elastic behaviour as seen in: **(a)** CVD-VACNTs showing an increase in the loss stiffness with increasing strains (Hutchens et al. 2012) (Copyright Wiley-VCH Verlag GmbH & Co. KGaA. Reproduced with permission) **(b)** CDC-VACNTs showing a significantly decrease in values of tan δ after buckling Reproduced from (Pathak et al. 2009) with permission from Elsevier. **(c)** Atomistic modelling image of a possible entangled arrangement of single, double and triple-walled CNTs leading to their rubber-like viscoelastic behaviour. Reprinted from (Gogotsi 2010) with permission from AAAS.

haviour in a random network of long, interconnected and tangled CNTs, similar in many ways to VACNTs but significantly less aligned, over a very wide temperature range – from -196°C to 1000°C, with a possibility of extending this behaviour beyond 1500°C. While the oxidizing nature of carbon may limit the application of these materials to only vacuum or protective (reducing) environments, CNTs are nevertheless the only known solids to demonstrate such behaviour at extremely low

or very high temperatures. The authors attribute the reversible dissipation of energy in CNTs over this remarkable range to the zipping and unzipping of the CNTs upon contact (see Fig. 8.10c) caused by the van der Waals interactions. In this instance, 'reversible' means that beyond a critical strain the zipping/unzipping process was no longer possible everywhere as more and more tubes become permanently entangled at higher strain. This would lead to a loss in their viscoelasticity, similar to the observations in the highly dense CDC-VACNTs (Fig. 8.10b).

The unique combination of superior mechanical properties and the ability to dissipate energy during deformation is expected to have significant implications in damping applications utilizing VACNTs. These, combined with the wide temperature range of its viscoelastic behaviour, make VACNT based materials a promising choice for use in mechanical applications under extreme temperatures or temperature gradients. Possible environments range from the cold of interstellar space to down-to-earth viscoelastic applications, such as MEMS devices to high temperature vacuum furnaces.

8.10. Applications

Multiwall carbon nanotubes are well known for a variety of exceptional properties. These include a high tensile modulus, on the order of 1 TPa, high strength, on the order of tens of GPa, high thermal conductivity, recoverability after large bending angle deformation, and a range of electrical properties depending on the chirality of the graphene walls. For these reasons they are currently the subject of a wide range of research. In the form of VACNTs, these individual tube properties may be significantly altered by the collective interaction of thousands of tubes. Several applications of VACNT structures currently under study rely on the mechanical behaviour described earlier in this chapter. A remarkable, but incomplete list includes: components of highly compliant thermal contacts for micro-electro-mechanical-systems (MEMS) and microelectronics (McCarter et al. 2006, Zbib et al. 2008), dry adhesives, thermally robust energy dissipating rubber (Gogotsi 2010, Xu et al. 2010), and energy absorption or impact mitigation (Misra 2008). Other applications, such as optical coatings and cold cathode arrays, may rely less on the mechanical properties for optimization and design, but understanding is still necessary for evaluation of robustness and in-use lifetime analysis.

We go through each application briefly to highlight the VACNT specific mechanical behaviour of interest. First, thermal contacts for delicate electronics devices have two requirements. They must be highly thermally conductive and make conformal contact (to increase heat transfer) while avoiding damage to the components they are transferring heat to and from. CNT foams are ideal for this application due to the high compliance that comes from the reduced load capacity of the CNT struts as they buckle. Dry adhesive applications of VACNTs take advantage of the hier-

archical structure which can, as desired in MEMS switches, make conformal contact to surfaces at a variety of roughness length scales, thereby increasing the attractive interactions between the tubes and the surface. Third, energy dissipating and absorbing applications require more in-depth knowledge of the deformation mechanism. As mentioned in the previous section, energy dissipation is currently thought to be due to tube zipping/unzipping or tube-to-tube sliding and rearrangement (Mesarovic et al. 2007, Suhr et al. 2007, Pathak et al. 2009, Gogotsi 2010, Xu et al. 2010), while energy absorption is certainly maximized during buckle formation. Future applications may be able to take advantage of yet undiscovered traits of the incompletely characterized VACNTs.

8.11. Summary and Outlook

Although the mechanisms governing VACNTs collective mechanical behaviour are still largely uncharacterized, the special properties of multiwall carbon nanotubes combined with the complex interactions that arise between them in the hierarchical VACNT microstructure have generated significant research interest. Their wide range of properties, mechanical, electrical, and thermal, make them ideal candidates as multi-functional materials, particularly for applications in which soft materials (such as polymers) have traditionally dominated. Notably, VACNTs occupy a unique niche among engineering materials as shown in the Ashby property chart in Fig. 8.11 with the ability to span a wide range of properties given a tunable microstructure. There remains two major hurdles to rationally designing VACNTs for any application: control of the CNT growth process and understanding of the relationship between the microstructure and mechanical response. These hurdles are interrelated through the fact that the design space cannot be systematically probed until the microstructure can be systematically controlled. Mastery of these unknowns will not only further VACNTs place as novel materials in the current applications under study, but may reveal previously undiscovered behaviours in microstructures yet to be created or characterized.
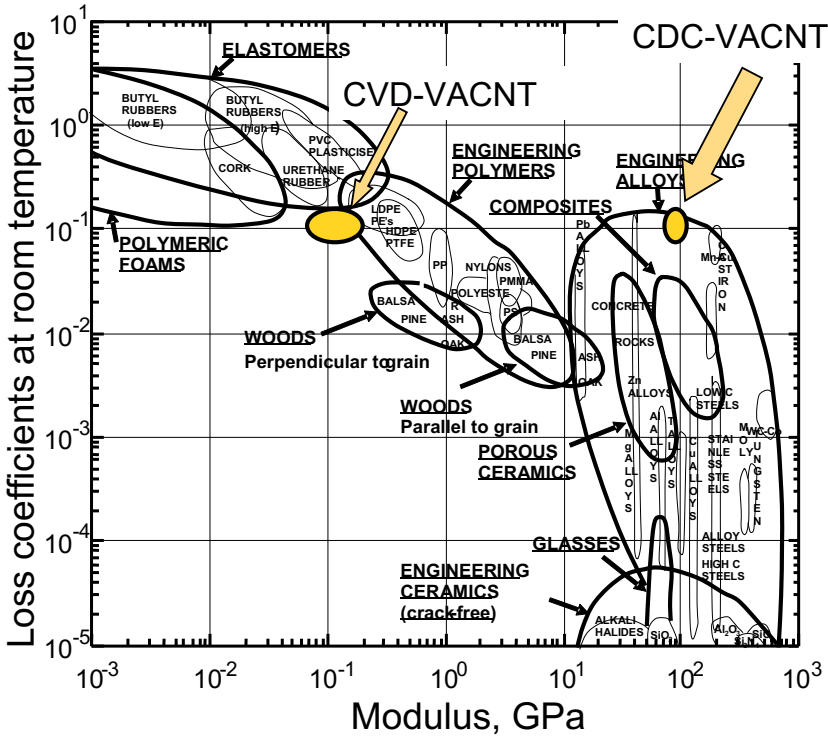
Figure 8.11. Ashby plot of Loss Coefficient vs. Modulus showing the performance of VACNTs.

Acknowledgements

References

Andrews, E. W., L. J. Gibson and M. F. Ashby (1999). "The creep of cellular solids." *Acta Materialia* 47(10): 2853-2863.

Andrews, E. W., G. Gioux, P. Onck and L. J. Gibson (2001). "Size effects in ductile cellular solids. Part II: Experimental results." *International Journal of Mechanical Sciences* 43(3): 701-713.

Andrews, R., D. Jacques, A. M. Rao, F. Derbyshire, D. Qian, X. Fan, E. C. Dickey and J. Chen (1999). "Continuous production of aligned carbon nanotubes: a step closer to commercial realization." *Chemical Physics Letters* 303(5-6): 467-474.

Astrom, J. A., A. V. Krasheninnikov and K. Nordlund (2004). "Carbon nanotube mats and fibers with irradiation-improved mechanical characteristics: A theoretical model." *Physical Review Letters* 93(21): 215503-215501-215503-215504.

Bedewy, M., E. R. Meshot, H. C. Guo, E. A. Verploegen, W. Lu and A. J. Hart (2009). "Collective Mechanism for the Evolution and Self-Termination of Vertically Aligned Carbon Nanotube Growth." *Journal of Physical Chemistry C* 113(48): 20576-20582.

Berhan, L., Y. B. Yi and A. M. Sastry (2004). "Effect of nanorope waviness on the effective moduli of nanotube sheets." *Journal of Applied Physics* 95(9): 5027-5034.

Bradford, P. D., X. Wang, H. Zhao and Y. T. Zhu (2011). "Tuning the Compressive Mechanical Properties of Carbon Nanotube Foam." *Carbon* 49(8): 2834-2841.

Brieland-Shoultz, A., S. Tawfick, S. J. Park, M. Bedewy, M. R. Maschmann, J. W. Baur and A. J. Hart (2014). "Scaling the Stiffness, Strength, and Toughness of Ceramic-Coated Nanotube Foams into the Structural Regime." *Advanced Functional Materials* 24(36): 5728-5735.

Cambaz, Z. G., G. Yushin, S. Osswald, V. Mochalin and Y. Gogotsi (2008). "Noncatalytic Synthesis of Carbon Nanotubes, Graphene and Graphite on SiC." *Carbon* 46(6): 841-849.

Cao, A., P. L. Dickrell, W. G. Sawyer, M. N. Ghasemi-Nejhad and P. M. Ajayan (2005). "Materials science: Super-compressible foamlike carbon nanotube films." *Science* 310(5752): 1307-1310.

Cao, C., A. Reiner, C. Chung, S.-H. Chang, I. Kao, R. V. Kukta and C. S. Korach (2011). "Buckling Initiation and Displacement Dependence in Compression of Vertically Aligned Carbon Nanotube Arrays." *Carbon* 49(10): 3190-3199.

Ci, L., J. Suhr, V. Pushparaj, X. Zhang and P. M. Ajayan (2008). "Continuous Carbon Nanotube Reinforced Composites." *Nano Letters* 8(9): 2762-2766.

Deck, C. P., J. Flowers, G. S. B. McKee and K. Vecchio (2007). "Mechanical Behavior of Ultralong Multiwalled Carbon Nanotube Mats." *Journal of Applied Physics* 101(2): 23512-23511-23519.

Deshpande, V. S. and N. A. Fleck (2000). "Isotropic constitutive models for metallic foams." *Journal of the Mechanics and Physics of Solids* 48(6-7): 1253-1283.

Fleck, N. A., H. Otoyo and A. Needleman (1992). "Indentation of porous solids." *International Journal of Solids and Structures* 29(13): 1613-1636.

Flores-Johnson, E. A. and Q. M. Li (2010). "Indentation into polymeric foams." *International Journal of Solids and Structures* 47(16): 1987-1995.

Fraternali, F., T. Blesgen, A. Amendola and C. Daraio (2011). "Multiscale mass-spring models of carbon nanotube foams." *Journal of the Mechanics and Physics of Solids* 59(1): 89-102.

Gibson, L. J. (2000). "Mechanical Behavior of Metallic Foams." *Annual Review of Materials Science* 30(Compendex): 191-227.

Gibson, L. J. and M. F. Ashby (1999). *Cellular Solids: Structure and Properties*. Cambridge, UK, Cambridge University Press.

Gogotsi, Y., Ed. (2006). *Nanotubes and Nanofibers*. Boca Raton, FL, CRC Press.

Gogotsi, Y. (2010). "High-Temperature Rubber Made from Carbon Nanotubes." *Science* 330(6009): 1332-1333.

Hutchens, S. and S. Pathak (2012). Vertically Aligned Carbon Nanotubes, Collective Mechanical Behavior. *Encyclopedia of Nanotechnology*, Springer. 22**:** 2809-2818.

Hutchens, S. B., L. J. Hall and J. R. Greer (2010). "In situ Mechanical Testing Reveals Periodic Buckle Nucleation and Propagation in Carbon Nanotube Bundles." *Advanced Functional Materials* 20(14): 2338-2346.

Hutchens, S. B., A. Needleman and J. R. Greer (2011). "Analysis of uniaxial compression of vertically aligned carbon nanotubes." *Journal of the Mechanics and Physics of Solids* 59(10): 2227-2237.

Johnson, K. L. (1987). *Contact Mechanics*, Cambridge University Press, Cambridge.

Kalidindi, S. R. and S. Pathak (2008). "Determination of the effective zero-point and the extraction of spherical nanoindentation stress–strain curves." *Acta Materialia* 56(14): 3523-3532.

Kis, A., G. Csanyi, J. P. Salvetat, T.-N. Lee, E. Couteau, A. J. Kulik, W. Benoit, J. Brugger and L. Forro (2004). "Reinforcement of single-walled carbon nanotube bundles by intertube bridging." *Nature Materials* 3(3): 153-157.

Kumar, M. and Y. Ando (2010). "Chemical vapor deposition of carbon nanotubes: A review on growth mechanism and mass production." *Journal of Nanoscience and Nanotechnology* 10(6): 3739-3758.

Kusunoki, M., M. Rokkaku and T. Suzuki (1997). "Epitaxial carbon nanotube film self-organized by sublimation decomposition of silicon carbide." *Applied Physics Letters* 71(18): 2620-2622.

Kusunoki, M., T. Suzuki, C. Honjo, T. Hirayama and N. Shibata (2002). "Selective synthesis of zigzag-type aligned carbon nanotubes on SiC (000-1) wafers." *Chemical Physics Letters* 366(5-6): 458-462.

Lu, Y. C., J. Joseph, Q. Zhang, M. R. Maschmann, L. Dai and J. Baur (2012). "Large-Displacement Indentation of Vertically Aligned Carbon Nanotube Arrays." *Experimental Mechanics* 52: 1551-1554.

McCarter, C. M., R. F. Richards, S. D. Mesarovic, C. D. Richards, D. F. Bahr, D. McClain and J. Jiao (2006). "Mechanical compliance of photolithographically defined vertically aligned carbon nanotube turf." *Journal of Materials Science* 41(23): 7872-7878.

Mesarovic, S. D., C. M. McCarter, D. F. Bahr, H. Radhakrishnan, R. F. Richards, C. D. Richards, D. McClain and J. Jiao (2007). "Mechanical Behavior of a Carbon Nanotube Turf." *Scripta Materialia* 56(2): 157-160.

Min-Feng, Y., O. Lourie, M. J. Dyer, K. Moloni, T. F. Kelly and R. S. Ruoff (2000). "Strength and breaking mechanism of multiwalled carbon nanotubes under tensile load." *Science* 287(5453): 637-640.

Misra, A. A. G., Julia R. AND Daraio, Chiara (2008). "Strain rate effects in the mechanical response of polymer-anchored carbon nanotube foams." *Advanced Materials* 20: 1-5.

Pantano, A., D. M. Parks and M. C. Boyce (2004). "Mechanics of deformation of single- and multi-wall carbon nanotubes." *Journal of the Mechanics and Physics of Solids* 52(4): 789-821.

Pathak, S., Z. G. Cambaz, S. R. Kalidindi, J. G. Swadener and Y. Gogotsi (2009). "Viscoelasticity and High Buckling Stress of Dense Carbon Nanotube Brushes." *Carbon* 47(8): 1969-1976.

Pathak, S. and S. R. Kalidindi (2015). "Spherical nanoindentation stress–strain curves." *Materials Science and Engineering: R: Reports* 91(0): 1-36.

Pathak, S., E. J. Lim, P. Pour Shahid Saeed Abadi, S. Graham, B. A. Cola and J. R. Greer (2012). "Higher Recovery and Better Energy Dissipation at Faster Strain Rates in Carbon Nanotube Bundles: An in-Situ Study." *ACS Nano* 6(3): 2189-2197.

Pathak, S., N. Mohan, E. Decolvenaere, A. Needleman, M. Bedewy, A. J. Hart and J. R. Greer (2013). "Local Relative Density Modulates Failure and Strength in Vertically Aligned Carbon Nanotubes." *ACS Nano* 7(10): 8593-8604.

Pathak, S., N. Mohan, P. Pour Shahid Saeed Abadi, S. Graham, B. A. Cola and J. R. Greer (2013). "Compressive Response of Vertically Aligned Carbon Nanotube Films gleaned from *In-Situ* Flat Punch Indentations." *Journal of*

Materials Research: Focus Issue on De Novo Carbon Nanomaterials 28(7): DOI: 10.1557/jmr.2012.1366.

Pathak, S., J. R. Raney and C. Daraio (2013). "Effect of morphology on the strain recovery of vertically aligned carbon nanotube arrays: An in situ study." *Carbon* 63: 303-316.

Poelma, R. H., B. Morana, S. Vollebregt, E. Schlangen, H. W. van Zeijl, X. Fan and G. Q. Zhang (2014). "Tailoring the Mechanical Properties of High-Aspect-Ratio Carbon Nanotube Arrays using Amorphous Silicon Carbide Coatings." *Advanced Functional Materials* 24(36): 5737-5744.

Pour Shahid Saeed Abadi, P., S. Hutchens, J. H. Taphouse, J. R. Greer, B. A. Cola and S. Graham (2012). "Effects of morphology on the micro-compression response of carbon nanotube forests." *Nanoscale* 4(11): 3373-3380.

Presser, V., M. Heon and Y. Gogotsi (2011). "Carbide-derived carbons - from porous networks to nanotubes and graphene." *Advanced Functional Materials* 21(5): 810-833.

Qi, H. J., K. B. K. Teo, K. K. S. Lau, M. C. Boyce, W. I. Milne, J. Robertson and K. K. Gleason (2003). "Determination of mechanical properties of carbon nanotubes and vertically aligned carbon nanotube forests using nanoindentation." *Journal of the Mechanics and Physics of Solids* 51: 2213-2237.

Qiu, A., D. F. Bahr, A. A. Zbib, A. Bellou, S. D. Mesarovic, D. McClain, W. Hudson, J. Jiao, D. Kiener and M. J. Cordill (2011). "Local and Non-Local Behavior and Coordinated Buckling of CNT Turfs." *Carbon* 49(4): 1430-1438.

Raney, J. R., F. Fraternali, A. Amendola and C. Daraio (2011). "Modeling and In Situ Identification of Material Parameters for Layered Structures Based on Carbon Nanotube Arrays." *Composite Structures* 93(11): 3013-3018.

Raney, J. R., A. Misra and C. Daraio (2011). "Tailoring the microstructure and mechanical properties of arrays of aligned multiwall carbon nanotubes by utilizing different hydrogen concentrations during synthesis." *Carbon* 49(Compendex): 3631-3638.

Ruoff, R. S., J. Tersoff, D. C. Lorents, S. Subramoney and B. Chan (1993). "Radial Deformation of Carbon Nanotubes by van der Waals Forces." *Nature* 364(6437): 514-516.

Salvetat, J.-P., S. Bhattacharyya and R. B. Pipes (2006). "Progress on Mechanics of Carbon Nanotubes and Derived Materials." *Journal of Nanoscience and Nanotechnology* 6(7): 1857-1882.

Sudheer Kumar, P., S. Ramchandra and U. Ramamurty (2003). "Effect of displacement-rate on the indentation behavior of an aluminum foam." *Materials Science and Engineering A* 347(1-2): 330-337.

Suhr, J., P. Victor, L. C. S. Sreekala, X. Zhang, O. Nalamasu and P. M. Ajayan (2007). "Fatigue Resistance of Aligned Carbon Nanotube Arrays under Cyclic Compression." *Nature Nanotechnology* 2(7): 417-421.

Tong, T., Y. Zhao, L. Delzeit, A. Kashani, M. Meyyappan and A. Majumdar (2008). "Height Independent Compressive Modulus of Vertically Aligned Carbon Nanotube Arrays." *Nano Letters* 8(2): 511-515.

Treacy, M. M. J., T. W. Ebbesen and J. M. Gibson (1996). "Exceptionally high Young's modulus observed for individual carbon nanotubes." *Nature* 381(6584): 678-680.

Waters, J. F., P. R. Guduru, M. Jouzi, J. M. Xu, T. Hanlon and S. Suresh (2005). "Shell buckling of individual multiwalled carbon nanotubes using nanoindentation." *Appl. Phys. Lett.* 87: 103109-103101-103103.

Waters, J. F., L. Riester, M. Jouzi, P. R. Guduru and J. M. Xu (2004). "Buckling Instabilities in Multiwalled Carbon Nanotubes under Uniaxial Compression." *Applied Physics Letters* 85(10): 1787-1789.

Xu, M., D. N. Futaba, T. Yamada, M. Yumura and K. Hata (2010). "Carbon Nanotubes with Temperature-Invariant Viscoelasticity from-196 degrees to 1000 degrees C." *Science* 330(6009): 1364-1368.

Xu, M., D. N. Futaba, M. Yumura and K. Hata (2011). "Carbon Nanotubes with Temperature-Invariant Creep and Creep-Recovery from −190 to 970 °C." *Advanced Materials* 23(32): 3686-3691.

Yaglioglu, O. (2007). *Carbon Nanotube Based Electromechanical Probes - PhD Thesis*. PhD, Massachusetts Institute of Technology.

Yaglioglu, O., A. Cao, A. J. Hart, R. Martens and A. H. Slocum (2012). "Wide Range Control of Microstructure and Mechanical Properties of Carbon Nanotube Forests: A Comparison Between Fixed and Floating Catalyst CVD Techniques." *Advanced Functional Materials* 22(23): 5028-5037.

Zbib, A. A., S. D. Mesarovic, E. T. Lilleodden, D. McClain, J. Jiao and D. F. Bahr (2008). "The Coordinated Buckling of Carbon Nanotube Turfs under Uniform Compression." *Nanotechnology* 19(17): 175704-175701-175707.

Zhang, Q., Y. C. Lu, F. Du, L. Dai, J. Baur and D. C. Foster (2010). "Viscoelastic Creep of Vertically Aligned Carbon Nanotubes." *Journal of Physics D-Applied Physics* 43(31): 315401-315401-315407.